Journal of Hazardous Materials 179 (2010) 141–150

Contents lists available at ScienceDirect

Journal of Hazardous Materials

journal homepage: www.elsevier.com/locate/jhazmat

Photocatalytic removal of NO and HCHO over nanocrystalline Zn_2SnO_4 microcubes for indoor air purification

Zhihui Ai[a,b,*], Shuncheng Lee[a,**], Yu Huang[a], Wingkei Ho[a], Lizhi Zhang[b]

[a] Department of Civil and Structural Engineering, Research Center for Environmental Technology and Management, The Hong Kong Polytechnic University, Hong Kong, People's Republic of China

[b] Key Laboratory of Pesticide & Chemical Biology of Ministry of Education of College of Chemistry, Central China Normal University, Wuhan 430079, People's Republic of China

ARTICLE INFO

Article history:
Received 16 November 2009
Received in revised form 23 January 2010
Accepted 20 February 2010
Available online 1 March 2010

Keywords:
Zn_2SnO_4
NO
HCHO
Photocatalysis

ABSTRACT

Nanocrystalline Zn_2SnO_4 microcubes were hydrothermally synthesized and systematically characterized by XRD, SEM, TEM, XPS, N_2 adsorption–desorption, and UV–vis DRS analysis. The resulting Zn_2SnO_4 microcubes with the edge size ranging from 0.8 to 1.2 μm were composed of numerous nanoparticles with size of 10–20 nm, and their optical band gap energy was estimated to be 3.25 eV from the UV–vis diffuse reflectance spectra. On degradation of nitrogen monoxide (NO) and formaldehyde (HCHO) at typical concentrations for indoor air quality, these nanocrystalline Zn_2SnO_4 microcubes exhibited superior photocatalytic activity to the hydrothermally synthesized ZnO, SnO_2, and Degussa TiO_2 P25, as well as C doped TiO_2 under UV–vis light irradiation. This enhanced photocatalytic activity of the nanocrystalline Zn_2SnO_4 microcubes was attributed to their bigger surface areas, smaller particle size, special porous structures, and special electronic configuration. The nanocrystalline Zn_2SnO_4 microcubes were chemically stable as there was no obvious deactivation during the multiple photocatalytic reactions. This work presents a promising approach for scaling-up industrial production of Zn_2SnO_4 nanostructures and suggests that the synthesized nanocrystalline Zn_2SnO_4 microcubes are promising photocatalysts for indoor air purification.

© 2010 Elsevier B.V. All rights reserved.

1. Introduction

Indoor air quality (IAQ) within buildings has been paid more and more attention with increasing awareness of the public environment and health, especially in urban cities, where metropolitan generally spend more than 80% of time in an indoor environment [1,2]. Gaseous pollutants such as NO_x, SO_2, carbonyl compounds, and volatile organic compounds (VOCs) are common hazardous species in indoor environment [3]. Among them, nitrogen oxides (NO_x) and formaldehyde (HCHO) are the representative omnipresent indoor air pollutants coming from the furnishings and decorating materials. For example, HCHO presents significant health effects as frequently causing cancer and other sickness, but the concentration of indoor HCHO usually might be at parts per billion (ppbv) to parts per million (ppmv) levels in China, which is much higher than the WHO guideline (80 ppbv) [4–6]. Therefore, a number of physical and chemical techniques, including physical adsorption, biofiltration, thermal catalysis, and photocatalytic oxidation, are well established for the purification of polluted air [3,7–9].

As an ambient temperature catalytic process, photocatalysis has gained considerable attention in view of solar energy conversion and water treatment, as well as air purification even at low concentrations. At moderate conditions, the photocatalysis can degrade a broad range of organic pollutants into innocuous final products such as CO_2 and H_2O [9]. To date, most of the studies are dominated by TiO_2 because of its chemical stability, low cost and relatively high activity. For instance, TiO_2 immobilized on different substrates, such as activate carbon and glass fibers, can photocatalytically degrade indoor air pollutants at parts per billion levels in a flow system under UV light irradiation [3,10–12]. However, the practical application of the TiO_2 photocatalytic process is restricted by the slow electron transfer rate and the low quantum efficiency [9]. Additionally, TiO_2 is prone to deactivation in the treatment of gaseous pollutants due to the deposition of the byproducts on its

* Corresponding author at: Key Laboratory of Pesticide & Chemical Biology of Ministry of Education of College of Chemistry, Central China Normal University, Wuhan 430079, People's Republic of China. Tel.: +852 2766 6011; fax: +852 2766 6011.

** Corresponding author at: Department of Civil and Structural Engineering, Research Center for Environmental Technology and Management, The Hong Kong Polytechnic University, Hong Kong, People's Republic of China. Tel.: +852 2766 6011; fax: +852 2766 6011.

E-mail addresses: jennifer.ai@mail.ccnu.edu.cn (Z. Ai), ceslee@polyu.edu.hk (S. Lee).

0304-3894/$ – see front matter © 2010 Elsevier B.V. All rights reserved.
doi:10.1016/j.jhazmat.2010.02.071

surface [13,14]. Therefore, it is appealing to develop novel photocatalysts that are active and stable enough for practical application.

Many approaches have been proposed to develop active and stable photocatalysts, including doping TiO_2 with metal ions or metal atoms, incorporating nitrogen and carbon into TiO_2, and employing other non-TiO_2 metal oxides as photocatalysts [15–24]. Non-TiO_2 photocatalysts have attracted a great deal of attentions because of their high photocatalytic efficiency and potential application in environmental remediation [25–29]. For instance, hierarchical BiOBr nanoplates were used to degrade NO pollutants at typical indoor air concentration previously, they exhibited high photocatalytic activity under UV–vis light irradiation [30].

As an n-type semiconductor, zinc stannate (Zn_2SnO_4) has been reported for its photocatalytical properties to produce H_2 or decompose organic pollutants in aqueous solution under the UV light irradiation [31–34]. Zn_2SnO_4 is usually prepared via solid-state or melting reactions, which could result in its inhomogeneity as well as low surface area. Many other approaches, including thermal evaporation, high temperature calcination, and sol–gel method, had been developed for the fabrication of nanostructured Zn_2SnO_4 [31–36]. Compared with the above processes, the hydrothermal method has been paid more interest due to its operational simplicity, cost-efficiency, and the capability for large-scale production. As expected, this approach could lead to crystalline products with pronounced photocatalytic performance.

In the present study, we reported a hydrothermal route to synthesize nanocrystalline Zn_2SnO_4 microcubes, and the resulting Zn_2SnO_4 microcubes were used for the degradation of typical indoor air pollutants. When compared with hydrothermally synthesized ZnO, SnO_2 counterparts, Degussa TiO_2 P25, as well as C doped TiO_2, the nanocrystalline Zn_2SnO_4 microcubes demonstrated an enhanced photocatalytic activity for the degradation of NO and HCHO at typical concentrations for indoor air quality under UV–vis light irradiation. In addition, the as-synthesized nanocrystalline Zn_2SnO_4 exhibited high photochemical stability in the degradation of NO under UV–vis light irradiation. This study presents a promising approach for scaling-up industrial production of Zn_2SnO_4 catalysts and suggests that the synthesized nanocrystalline Zn_2SnO_4 microcubes are potential photocatalysts for indoor air purification.

2. Experimental

2.1. Synthesis

All chemicals in this study were of commercially available analytical grade. Deionized water was used in all experiments. The nanocrystalline Zn_2SnO_4 microcubes were synthesized via a hydrothermal route. In a typical procedure, 2 mmol of $SnCl_4{\cdot}5H_2O$ and 4 mmol of $ZnSO_4{\cdot}7H_2O$ were dissolved into 35 mL of deionized water to form two transparent solutions, respectively. The two solutions were mixed together, and then 2 g of cellulose acetate (CA) was added to the above mixture under vigorous magnetic stirring for 10 min. Then 0.5 M NaOH solutions were added dropwise into the above mixed solution until the pH of the suspension was adjusted to 10 under magnetic stirring. The white suspension obtained was transferred to a 100 mL Teflon-lined stainless steel autoclave and heated at 220 °C for 48 h. After the autoclave was cooled naturally to room temperature, the final precipitates were filtered and washed repeatedly with distilled water and absolute alcohol and dried in air at 60 °C. For comparison to the resulting nanocrystalline Zn_2SnO_4 microcubes, ZnO and SnO_2 counterparts were also prepared at the absence of $SnCl_4{\cdot}5H_2O$ or $ZnSO_4{\cdot}7H_2O$ using the same hydrothermal synthesis route following a calcination at 500 °C for 4 h, respectively.

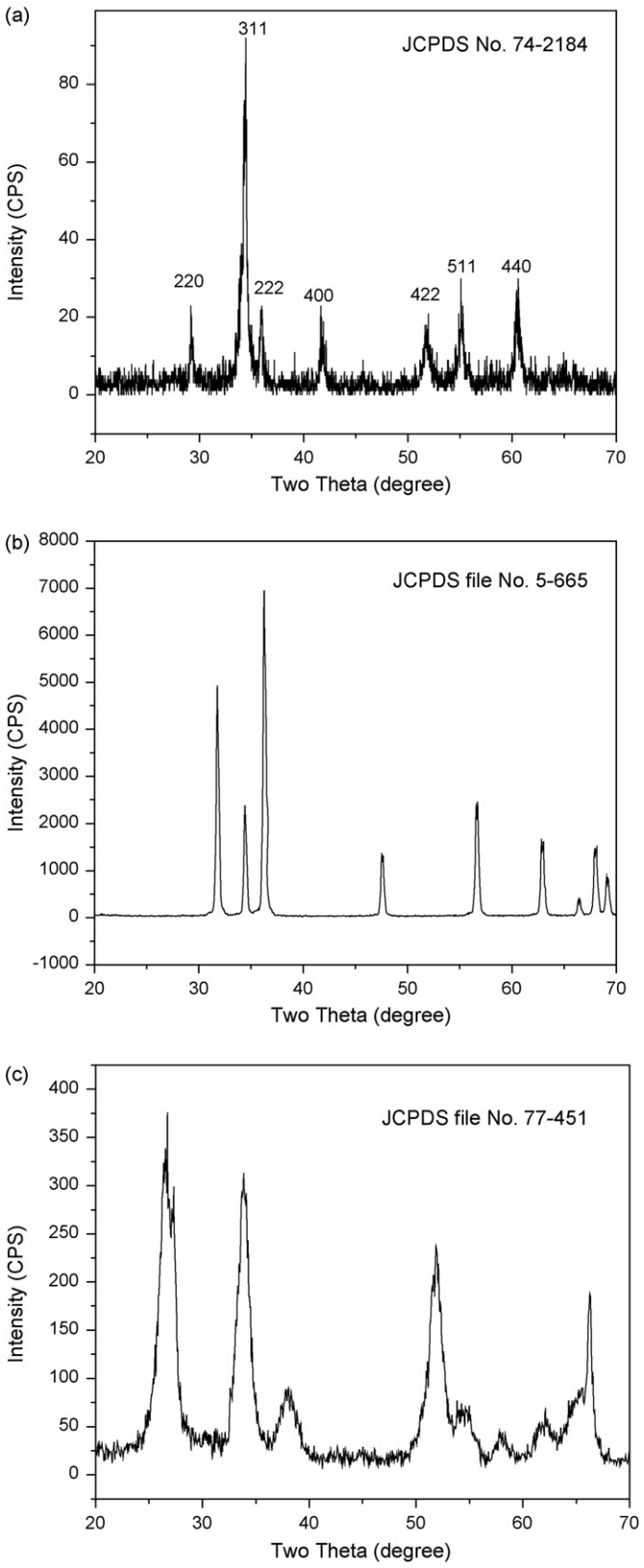

Fig. 1. XRD patterns of the as-prepared samples. Zn_2SnO_4 microcubes (a); ZnO (b); and SnO_2 (c).

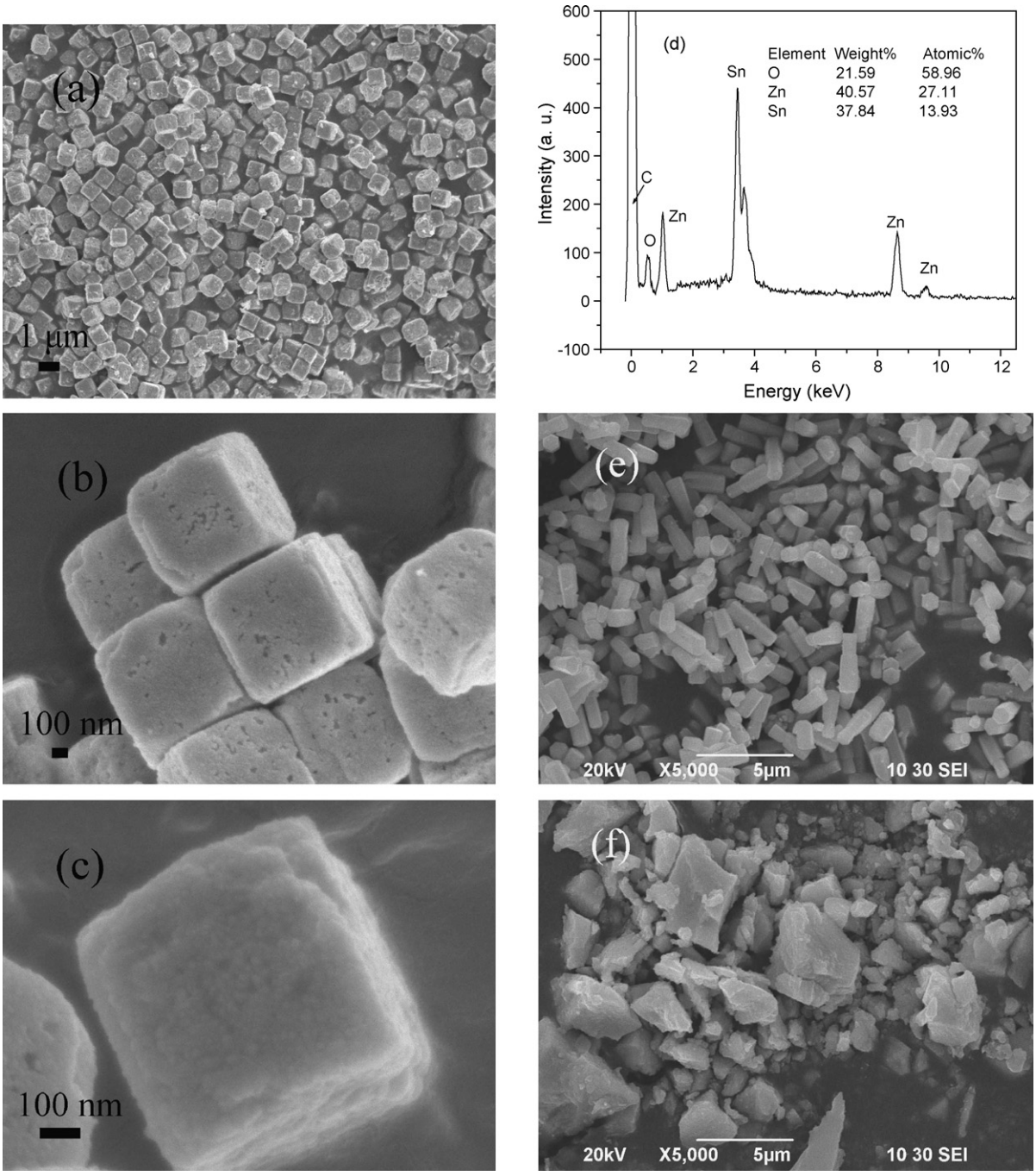

Fig. 2. SEM images at low magnification (a, b) and high magnification (c), EDX pattern (d) of the resulting Zn_2SnO_4 samples; SEM images of the hydrothermally synthesized ZnO (e) and SnO_2 (f), respectively.

2.2. Characterizations

X-ray powder diffraction patterns were obtained on a Broker D8 Advance X-ray diffract meter with Cu Ka radiation (λ = 1.54178 Å). Scanning electron microscopy images were recorded on a LEO 1450VP scanning electron microscope. Transmission electron microscopy (TEM) study was carried out on a Philips CM-120 electron microscope. The samples for TEM were prepared by dispersing the final powders in ethanol; the dispersion was then dropped on carbon–copper grids. Furthermore, the obtained powders deposited on a copper grid were observed by a high-resolution transmission electron microscope (HRTEM; JEOL JSM-2010 microscope) operating at 200 kV. UV–vis diffuse reflectance spectra were recorded on the Cary 300 UV–vis spectrophotometer equipped with an integrated sphere at room temperature. X-ray photoemission spectroscopy (XPS) spectra were recorded on a PHI 5600 multi-technique system with a monochromatic Al Kα source (Physical Electronics) operated at 150 W (15 kV, 10 mA). The nitrogen adsorption and desorption isotherms at 77 K were measured using a Micromeritics ASAP2010 system after samples were vacuum-dried at 473 K overnight.

2.3. Photocatalytic experiments

The photocatalytic experiments on the resulting samples for degradation of NO and HCHO at typical concentrations for indoor

air quality were performed at ambient temperature in a continuous flow reactor. The volume of the rectangular reactor which was made of stainless steel and covered with Saint-Glass was 4.5 L (10 cm × 30 cm × 15 cm ($H \times L \times W$)). One dish containing the 0.2 g of photocatalyst powders was placed in the middle of the reactor. A 300 W commercial tungsten halogen lamp (General Electric) was used as the UV–vis light source. The lamp was vertically placed outside the reactor above the sample dish. Four mini-fans were fixed around the lamp to avoid the temperature rise of the flow system. The integrated UV intensity in the range 310–400 nm was $720 \pm 10\ \mu W/cm^2$. The photocatalyst samples were prepared by coating an aqueous suspension of the resulting samples onto a dish with a diameter of 5.0 cm. The dishes containing the photocatalyst were pretreated at 70 °C until complete removal of water in the suspension and then cooled to room temperature. NO and HCHO gas were selected as the target pollutant for the photocatalytic degradation at ambient temperature. The NO gas was acquired from a compressed gas cylinder at a concentration of 48 ppm NO (N_2 balance, BOC gas) with traceable National Institute of Stands and Technology (NIST) standard. The HCHO gas was obtained from Linde Canada Limited at a concentration of 100 ppm. The initial concentration of NO and HCHO were diluted to about 400 ppb and 2 ppm by the air stream supplied by a zero air generator (Thermo Environmental Inc., Model 111), respectively. The desired humidity level of the NO and HCHO flow was controlled at 70% (2100 ppmv) by passing the zero air streams through a humidification chamber. The gas streams were premixed completely by a gas blender, and the flow rate was controlled at 4 L min^{-1} by a mass flow controller. After the adsorption–desorption equilibrium among water vapor, gases, and photocatalysts was achieved, the lamp was turned on. The concentration of NO was continuously measured by a chemiluminescence NO analyzer (Thermo Environmental Instruments Inc., Model 42c), which monitors NO and NO_2 with a sampling rate of 0.7 L/min. The removal rate (%) of NO was the ratio of the concentration of NO in the feeding stream and the concentration of NO_x (NO and NO_2) in the outlet stream. The reaction of NO with air was ignorable when performing a control experiment with or without light in the absence of photocatalyst.

As per the HCHO analysis, firstly, an acidified 2,4-dintrophenylhydrazine (Waters Sep-Pak DNPH-silica) equipped with a Desert Research Institute (DRI)'s standard carbonyl sampler was used to collect the HCHO according to the USEPA TO-11 method. After sampling, all the cartridges were capped and wrapped in pouches provided by Waters. The pouches were stored in a refrigerator at −10 °C and were analyzed within 1 week. The cartridge was then eluted with 5 mL of acetonitrile (HPLC grade). At last, the DNPH-carbonyl derivatives were analyzed by injecting 20 μL of the sample into a high performance liquid chromatography (HPLC, Perkin Elmer Series 200). The HPLC system consisted of a dual wavelength absorbance detector (Perkin Elmer UV/VIS) operating at 365 nm with a binary pump (Perkin Elmer Series 200) and an in-line degasser. A nova-Pak (Waters) C18 reverse phase column (150 mm × 3.9 mm) with a particle size of 4 mm and pore size of 60 Å was used to separate the hydrazones. The use of the reverse phase column is to facilitate the separation of HCHO from other aliphatic hydrazones since the hydrazones are eluted in the order of decreasing polarity. The mobile phase consisted of two solvent mixtures, namely mixture A: 6:3:1 (v/v) of water/acetonitrile/tetrahydrofuran; and mixture B: 4:6 (v/v) of water/acetonitrile. The gradient program is 100% A for 1 min, followed by a linear gradient from 100% A to 100% B in 10 min. The flowrate is 1.5 mL/min. The HCHO concentration was calibrated by a standard purchased from Superco (CARB Method 1004 DNPH Mix 2). The removal rate (%) of HCHO was the ratio of the concentration of HCHO in the feeding stream and the concentration of HCHO in the outlet stream.

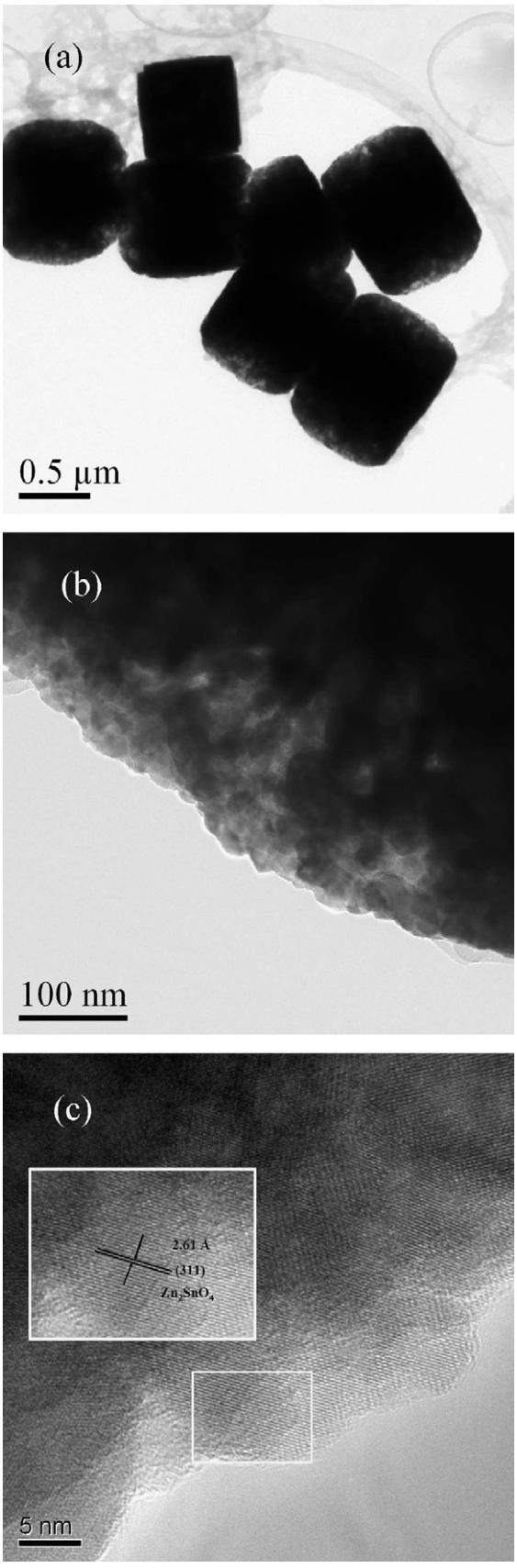

Fig. 3. TEM at low magnification (a) and high magnification (b), and HRTEM images (c) of the resulting Zn_2SnO_4 samples.

3. Results and discussion

3.1. XRD patterns of the as-prepared samples

The power X-ray diffraction (XRD) pattern provides crystallinity and phase structures information for the obtained samples (Fig. 1). All the diffraction peaks in the XRD pattern can be indexed to cubic Zn_2SnO_4 with a lattice parameter $a = 8.65$ nm according to the standard XRD data file (JCPDS File No. 74-2184) (Fig. 1a). The diffraction peaks at 2θ values of 29.24°, 34.42°, 35.93°, 41.72°, 51.89°, 55.21°, and 60.57° can be ascribed to the reflection of (2 2 0), (3 1 1), (2 2 2), (4 0 0), (4 2 2), (5 1 1), and (4 4 0) planes of the cubic Zn_2SnO_4, respectively. The broad peaks indicate the nanocrystalline nature of the materials. Estimated from the prominent (3 1 1) reflection using the Scherrer's equation, the average crystallite size of the Zn_2SnO_4 crystals was about 15 nm. No other impurity phases such as ZnO, SnO_2 were found, indicating the good phase purity of the cubic Zn_2SnO_4 products. The chemical mechanism for hydrothermal formation of the nanocrystalline Zn_2SnO_4 can be expressed in Eqs. (1) and (2). Prior to the hydrothermal process, $Zn(OH)_2$ and $Sn(OH)_4$ precipitates are formed (Eq. (1)). During the hydrothermal stage, Zn_2SnO_4 crystals are formed from the $Zn(OH)_2$ and $Sn(OH)_4$ precipitates using NaOH as the alkaline mineralizer (Eq. (2)). Cellulose acetate could serve as a surfactant during the hydrothermal process. In addition, as shown in Fig. 1b and c, ZnO (JCPDS File No. 5-665) and SnO_2 (JCPDS File No. 77-451) counterparts were also obtained at the absence of $SnCl_4{\cdot}5H_2O$ or $ZnSO_4{\cdot}7H_2O$ using the same hydrothermal method, respectively.

$$2Zn^{2+} + Sn^{4+} + 8OH^- \rightarrow 2Zn(OH)_2 + Sn(OH)_4 \quad (1)$$

$$2Zn(OH)_2 + Sn(OH)_4 \rightarrow Zn_2SnO_4 + 4H_2O \quad (2)$$

3.2. SEM and TEM images of the as-prepared samples

The morphology of the resulting samples was investigated by scanning electron microscopy (SEM) (Fig. 2). As seen in the typical SEM image at low magnification (Fig. 2a), the general morphology of the as-synthesized Zn_2SnO_4 product is monodispersed and regular uniform cube-shaped with a width size ranging from 0.8 to 1.2 μm. The SEM images at high magnification show that the surfaces of these Zn_2SnO_4 microcubes are rough and porous as they comprised of numerous nanoparticles, these nanoparticles contact closely and therefore many porous holes can be observed (Fig. 2b and c). Furthermore, energy dispersive X-ray (EDX) spectroscopy analysis reveals that carbon, zinc, tin, and oxygen elements coexist in the synthesized Zn_2SnO_4 microcubes (Fig. 2d), where carbon comes from the surface adventitious carbon from atmosphere and the conductive adhesive tape for SEM measurement. The average atomic ratio of Zn/Sn/O is 1.95:1:4.23 (inset of Fig. 2d), indicating the product is oxygen-rich. The excess oxygen might arise from the surface OH, adsorbed H_2O, and carbonate species on the surface. The results of XRD, SEM and EDX indicated nanocrystalline

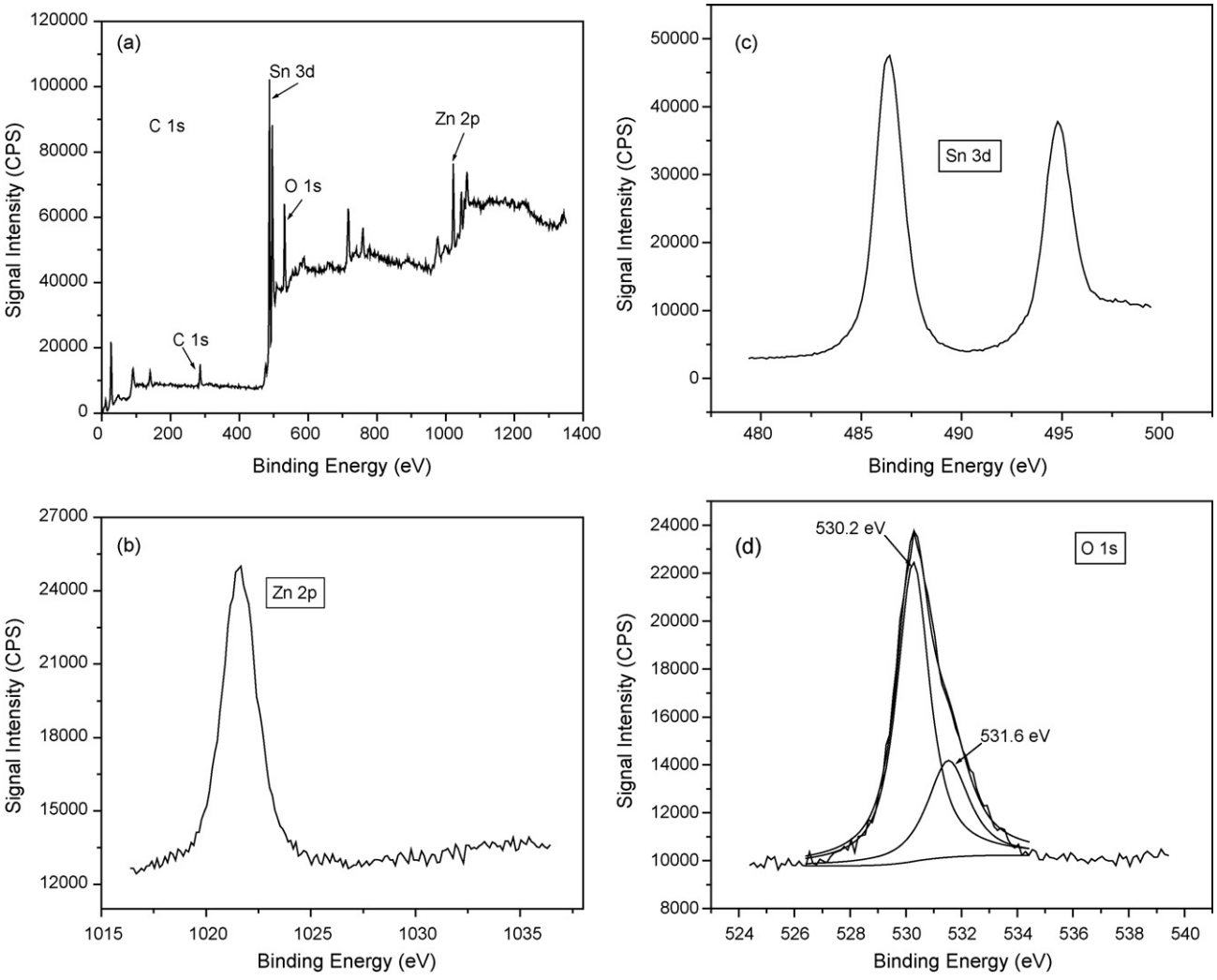

Fig. 4. XPS spectra of the resulting Zn_2SnO_4 samples, survey (a); and high resolution spectra of Zn 2p (b), Sn 3d (c), O1s (d).

Zn_2SnO_4 microcubes could be obtained via this facile hydrothermal method. For comparison, the morphologies of the hydrothermally synthesized ZnO and SnO_2 are shown in Fig. 2e and f, respectively. Different from the cubic shape of as-prepared Zn_2SnO_4, the ZnO samples are solid stick-like, while the SnO_2 samples are irregular bulk particles.

Transmission electron microscopy (TEM) and high-resolution transmission electron microscopy (HRTEM) were used to further investigate the crystal structure and morphology of these nanocrystalline Zn_2SnO_4 microcubes (Fig. 3). It was observed that the as-prepared Zn_2SnO_4 were monodispersed cubes with the edge size ranging from 0.8 to 1.2 μm (Fig. 3a). These Zn_2SnO_4 microcubes consist of a number of small crystallites with a diameter between 10 and 20 nm (Fig. 3b). These small crystalline particles contact closely and originate interparticle porosity, indicating the porous nature of nanocrystalline Zn_2SnO_4 microcubes. In order to investigate the nanocrystalline nature of Zn_2SnO_4 microcubes, the sample was characterized by HRTEM (Fig. 3c). HRTEM image reveals that the Zn_2SnO_4 microcubes are architecturally porous. The particle sizes of the nanoparticles on the surface are in the range of 10–20 nm. The lattice spacing between adjacent lattice planes is about 2.61 Å, which corresponds to the interplanar spacing of the (3 1 1) plane of the cubic phase of Zn_2SnO_4 (JCPDS File No. 74-2184).

3.3. XPS spectra and BET specific surface area of the as-prepared samples

X-ray photoelectron spectroscopy (XPS) was further used to probe the surface chemical compositions and its chemical oxidation state of the as-prepared nanocrystalline Zn_2SnO_4 microcubes (Fig. 4). As shown from the survey spectra in Fig. 4a, element Zn, Sn, O and C coexisted in the samples, where the carbon peaks are attributed to the residual carbon from the sample and adventitious hydrocarbon from XPS instrument itself. The Zn 2p spectrum confirms of the presence of Zn element in the products (Fig. 4b). The binding energies of Sn $3d_{5/2}$ and Sn $3d_{3/2}$ are indexed to 486.3 and 494.8 eV, respectively (Fig. 4c). Meanwhile, O 1s spectra of the samples obtained at different time were also recorded (Fig. 4d). The broad peak of O 1s can be fitted to two peaks at binding energies of 530.2 and 531.6 eV respectively by using a Gaussian fitting method. The dominant peak at 530.2 eV is characteristics of oxygen in metal oxide such as Sn–O–Zn, and the other peak at around 531.6 eV is assigned to other oxygen components such as OH, H_2O and carbon-

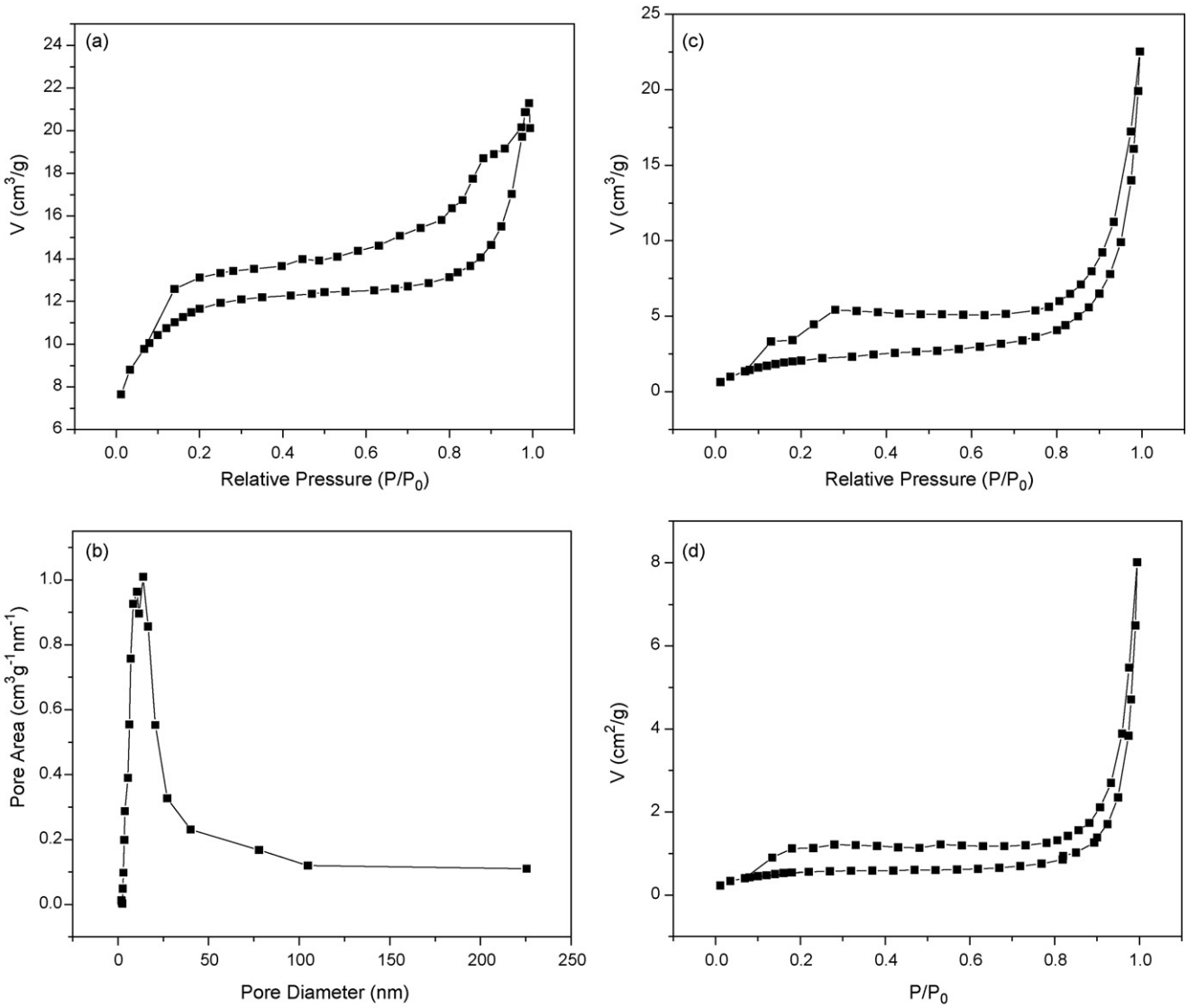

Fig. 5. N_2 adsorption–desorption isotherms (a) and Barret–Joyner–Halenda (BJH) pore size distribution plots (b) of the nanocrystalline Zn_2SnO_4 microcubes; N_2 adsorption–desorption isotherms of the prepared ZnO (e) and SnO_2 (f), respectively.

ate species adsorbed on the surface of Zn_2SnO_4. The results of XPS are consistent with XRD and HRTEM results.

Fig. 5 shows the nitrogen adsorption/desorption isotherm and pore size distribution curve of the resulting nanocrystalline Zn_2SnO_4 microcubes. The physioadsorption isotherms can be classified as type IV in the IUPAC classification with a distinct hysteresis loop, which was characteristic of porous materials. The Brunauer–Emmett–Teller (BET) specific surface area of the sample was 41.24 $m^2\,g^{-1}$. Fig. 5b shows the Barrett–Joyner–Halenda (BJH) pore size distribution plot for N_2-sorption isothermals for the resulting Zn_2SnO_4 product. The BJH analysis showed that the nanocrystalline Zn_2SnO_4 microcubes possessed pores with a mean diameter around 16 nm. These results are consistent with the XRD result and the observation in TEM image. However, the BET surface areas of the prepared ZnO and the SnO_2 counterparts are only 8.81 and 2.59 $m^2\,g^{-1}$, respectively (Fig. 5c and d), which are much lower than that of nanocrystalline Zn_2SnO_4 microcubes.

3.4. UV–vis DRS spectra of the as-prepared samples

We studied the optical absorption of the nanocrystalline Zn_2SnO_4 microcubes to estimate their energy band gaps (Fig. 6). It was found that nanocrystalline Zn_2SnO_4 microcubes presented strong photoabsorption properties in the UV light region (Fig. 6a). The steep shape of the spectra indicated that the light absorption was not due to the transition from the impurity level but was due to the band gap transition. The absorption band gap energy, E_g, can be determined by Eq. (3).

$$(\alpha h\nu)^n = K(h\nu - E_g) \quad (3)$$

where $h\upsilon$ is the photoenergy, α is the absorption coefficient, K is a constant relative to the material. And n decides the characteristics of the transition in a semiconductor. The energy band gaps of Zn_2SnO_4 cubes could be estimated from the tangent line in the plot of the square root of Kubelka–Munk functions against photon energy (Fig. 6b). The tangent line, which is extrapolated to $(\alpha h\upsilon)^{1/2} = 0$, indicates the band gap of the Zn_2SnO_4 cubes is about 3.25 eV. This calculated band gap is narrower than 3.6 eV reported in literatures due to its nanocrystalline nature [32–34].

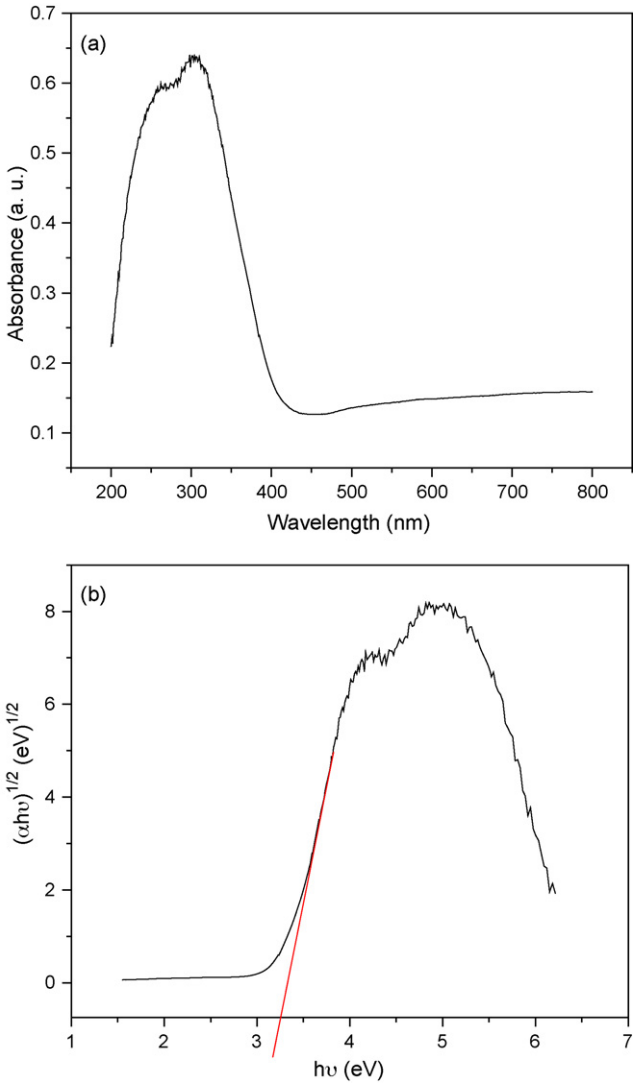

Fig. 6. UV–vis diffuse reflectance absorption spectra (a), and the plots of $(\alpha h\upsilon)^{1/2}$ vs photon energy ($h\upsilon$) (b) of the resulting Zn_2SnO_4 samples.

3.5. Photocatalytic degradation of NO and HCHO

The nanocrystalline Zn_2SnO_4 microcubes were used to photocatalytically degrade NO and HCHO at typical concentrations for indoor air quality in order to demonstrate their potential indoor air purification application (Fig. 7). Fig. 7a shows the variation of NO concentration (C/C_0) with irradiation time. Here, C_0 is the initial concentration of NO, and C is the concentration of NO_x after photocatalytic degradation for t. As a comparison, direct photolysis of NO, and photocatalytic oxidation of NO on ZnO and SnO_2 counterparts were also performed under identical conditions. As shown in Fig. 7a, NO could not be photolysed under UV–vis light irradiation. Obviously, compared with ZnO and SnO_2, the nanocrystalline Zn_2SnO_4 microcubes showed higher photocatalytic activity under UV–vis light and their NO removal rate reached 69.9%, however, the degradation of NO on the ZnO and SnO_2 were only 42.1% and 33.1%, respectively. The NO removal efficiency of the nanocrystalline Zn_2SnO_4 microcubes was also much higher than the famous photocatalyst Degussa TiO_2 P25, which could only remove 8% NO in 10 min under simulated solar light irradiation [3,30]. Moreover, the photocatalytic activity of the nanocrystalline Zn_2SnO_4 microcubes was even significantly higher than that of C-doped TiO_2 (25% of NO removal in 10 min) [3,30].

For a clearly quantitative comparison, we used the Langmuir–Hinshelwood model (L–H) to describe the rates of photocatalytic oxidation of NO on nanocrystalline Zn_2SnO_4 microcubes [37]. The initial photocatalytic degradation of NO was found to follow mass-transfer-controlled first-order kinetics approximately as a result of low concentration target pollutants, as evidenced by the linear plot of $\ln(C/C_0)$ versus photocatalytic reaction time t. The initial rate constant of the NO degradation over the nanocrystalline Zn_2SnO_4 microcubes under UV–vis light irradiation was estimated to be 0.0829 min^{-1}. This constant is significantly higher than that over the ZnO (0.0693 min^{-1}) and SnO_2 (0.0507 min^{-1}) counterparts (Fig. 7b). The photocatalytic oxidation of gaseous NO has been proposed to involve reactions displayed in Eqs. (4)–(7). Nitrogen monoxide reacted with reactive radicals to produce HNO_2 and HNO_3 [30].

$$NO + 2{\cdot}OH \rightarrow NO_2 + H_2O \quad (4)$$

$$NO_2 + {\cdot}OH \rightarrow NO_3^- + H^+ \quad (5)$$

$$NO + NO_2 + H_2O \rightarrow 2HNO_2 \quad (6)$$

$$NO_x + {\cdot}O_2^- \rightarrow NO_3^- \quad (7)$$

In the present study, the inlet HCHO concentration was conditioned to 2 ppm as it is the common level in "sick buildings". HCHO could not be photolysed under simulated solar light irradiation. The typical plots describing the decrease in the concentration of

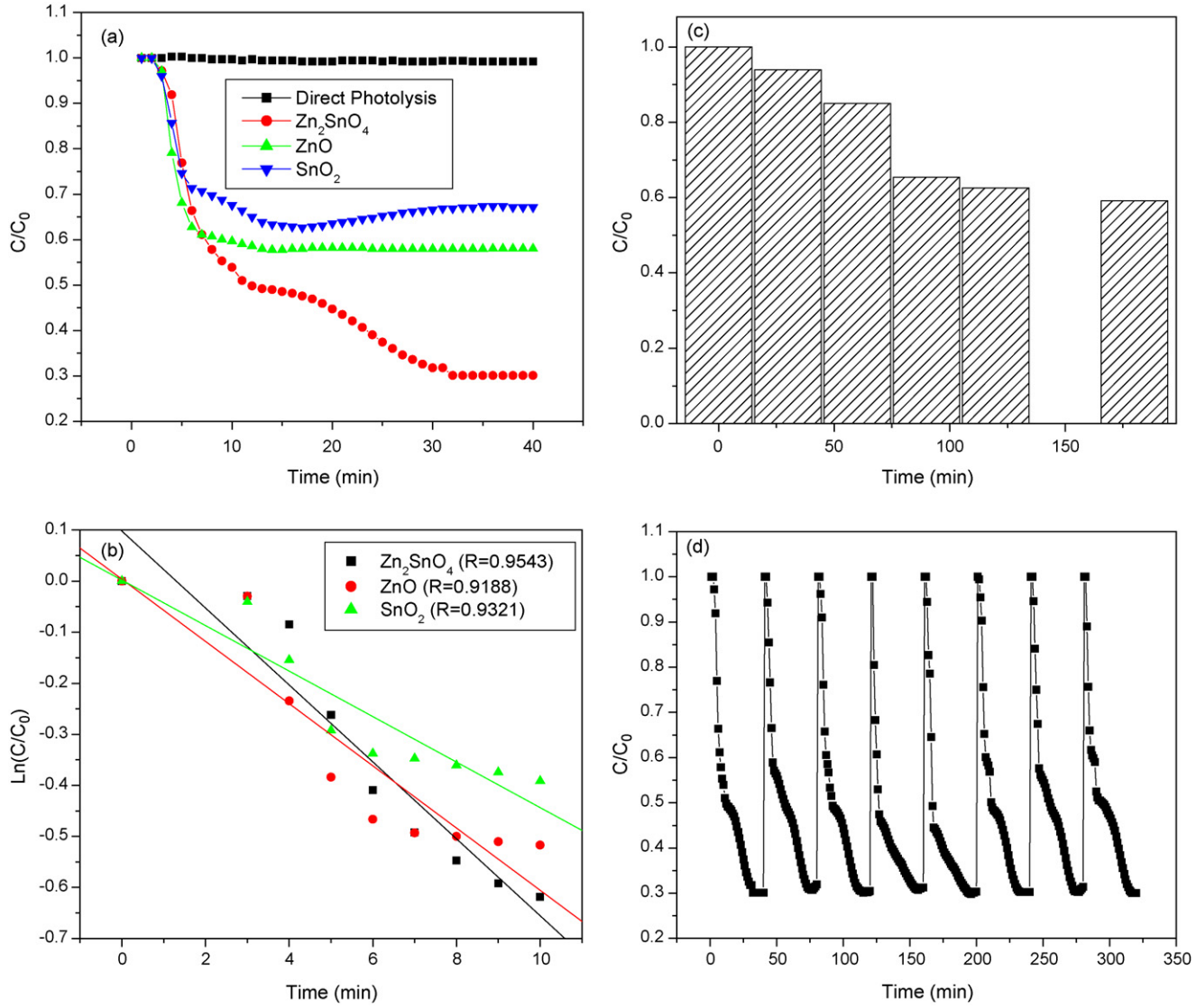

Fig. 7. Plots of the UV–vis light induced decrease in NO_x concentration vs irradiation time in the presence of nanocrystalline Zn_2SnO_4 microcubes, ZnO, SnO_2 counterpart, and the photolysis of NO (a); dependence of $\ln(C/C_0)$ on irradiation time in the presence of nanocrystalline Zn_2SnO_4 microcubes, ZnO, SnO_2 counterpart for degradation of NO (b); plots of the decrease in HCHO concentration vs irradiation time in the presence of nanocrystalline Zn_2SnO_4 microcubes (c); and the stability of nanocryatalline Zn_2SnO_4 microcubes in multiple runs of degradation of NO (d).

formaldehyde as a function of reaction time are shown in Fig. 7c. The photodegradation of HCHO on the nanocrystalline Zn_2SnO_4 microcubes was 26.4%, suggesting that the resulting Zn_2SnO_4 catalysts could be used for air purification. The photocatalytic oxidation of gaseous formaldehyde has been proposed to involve a carbonyl-radical-mediated chain reaction, which is mediated by hydroxyl radicals, superoxide radicals, and/or hydrogen peroxide. Under a specific illumination, if the number of HCHO molecules adsorbed on Zn_2SnO_4 surface is much larger than the number of photogenerated holes on the Zn_2SnO_4 surface, most of the absorbed HCHO molecules will be oxidized to formic acid (Eq. (8)). When the number of the holes photogenerated on Zn_2SnO_4 surface is much larger than the number of the adsorbed HCHO molecules, the proportion of mineralization of HCHO to CO_2 might increase (Eq. (9)) [38].

$$HCHO + H_2O + h^+ \rightarrow HCOOH + H^+ \quad (8)$$

$$HCHO + H_2O + h^+ \rightarrow CO_2 + H^+ \quad (9)$$

Generally, the overall photocatalytic activity of a semiconductor is primarily decided by its adsorption ability, structure, morphology, and electronic configuration. This enhanced photocatalytic activity of the nanocrystalline Zn_2SnO_4 microcubes could be attributed to its porous structure with a high surface area, smaller particle size, special porous structures, and special electronic configuration. Firstly, the porous structure of the Zn_2SnO_4 microcubes was favorable for the diffusion of intermediates and could enhance the photocatalytic activity. Secondly, the specific surface area of Zn_2SnO_4 calculated by the BET method was 41.24 $m^2\,g^{-1}$, while the specific surface area of the ZnO and SnO_2 counterparts were merely 8.81 and 2.59 $m^2\,g^{-1}$, respectively (see Fig. 5), the activity enhancement of nanocrystalline Zn_2SnO_4 microcubes should be attributed to their large specific surface area. Thirdly, the nanocrystalline Zn_2SnO_4 microcubes has possessed a high photoabsorption coefficient in the UV light region (see Fig. 6), indicating that the as-prepared nanocrystalline Zn_2SnO_4 microcubes can utilize UV–vis light effectively. Fourthly, in addition to the porous morphology and large surface area, its special electronic configuration and intrinsic oxygen vacancy may also be responsible for the high photocatalytic activity of Zn_2SnO_4. The wide band gap of Zn_2SnO_4 endows the photogenerated holes and electrons with strong redox ability. For

the ternary semiconductors, the conduction band is usually highly dispersive because of the hybridization of the orbitals, which promotes the mobility of the photogenerated electrons, leading to the enhancement of charge separation [39].

All those photocatalysts contain a central metal ion with d^{10} or d^0 electronic configuration, which has been reported to be favorable for the separation of photogenerated electron/hole pairs. The stability of a photocatalyst is important for its practical application. It was reported that the N-doped TiO_2 and sulfide photocatalysts sometimes suffer from instability under repeated use. Comparing with aqueous-phase photocatalytic reaction, an important disadvantage existing in gas-phase photocatalytic reactions is that the intermediates generated by photocatalysis would accumulate on the surface of the photocatalyst to deactivate the photocatalyst during the photocatalytic process in the gas phase, while water is able to remove reaction intermediates from the photocatalyst surface in aqueous-phase photocatalytic reaction system, which can alleviate the deactivation of photocatalyst [40,37].

To further study the stability of the nanocrystalline Zn_2SnO_4 microcubes on photocatalytic oxidation of NO in gas phase, we carried out the multiple runs of photocatalytic experiment with the used Zn_2SnO_4 microcubes (Fig. 7d). It was interesting to find the Zn_2SnO_4 microcubes catalyst only exhibited slight deactivation after eight cycles of repeated experiments, suggesting that the Zn_2SnO_4 microcubes are promising for indoor air purification under UV–vis light irradiation.

4. Conclusions

In summary, nanocrystalline Zn_2SnO_4 microcubes were hydrothermally synthesized and used to remove NO and HCHO in indoor air under UV–vis light irradiation. On degradation of NO at 400 ppb and HCHO at 2 ppm level, which are typical concentrations for indoor air quality, the nanocrystalline Zn_2SnO_4 exhibited superior photocatalytic activity to the hydrothermally synthesized ZnO and SnO_2 counterpart powders, and Degussa TiO_2 P25 as well as C doped TiO_2. The excellent catalytic activity and the stability of the nanocrystalline Zn_2SnO_4 microcubes were attributed to their special microporous structure with large surface areas and special electronic configuration. The porous structure is favorable for the diffusion of intermediates and final products of NO/HCHO oxidation, meanwhile, the special electronic configuration is responsible for the better charge separation. This work suggests that the nanocrystalline Zn_2SnO_4 microcubes are promising photocatalytic materials for indoor air purification.

Acknowledgements

This work was supported by the Hong Kong Polytechnic University (GYX0L, G-u712), the Research Grants Council of Hong Kong (Poly U 5204/07E), National Science Foundation of China (Grants 20977039 and 20777026), Program for Distinguished Young Scientist of Hubei Province (2009CDA014), Program for Innovation Team of Hubei Province (2009CDA048), Self-Determine Research Funds of CCNU from the Colleges' Basic Research and Operation of MOE (CCNU09A02014, CCNU09C01009), National Basic Research Program of China (973 Program) (Grant 2007CB613301), Program for New Century Excellent Talents in University (Grant NCET-07-0352), and the Key Project of Ministry of Education of China (Grant 108097).

References

[1] S.L. Fischer, C.P. Koshland, Daily and peak 1 h indoor air pollution and driving factors in a rural Chinese village, Environ. Sci. Technol. 41 (2007) 3121–3126.
[2] L.S.R. Brickus, J.N. Cardoso, F.R. de Aquino Neto, Distributions of indoor and outdoor air pollutants in Rio de Janeiro, Brazil: implications to indoor air quality in bayside offices, Environ. Sci. Technol. 32 (1998) 3485–3490.
[3] Y. Huang, W.K. Ho, S.C. Lee, L.Z. Zhang, G.S. Li, J.C. Yu, Effect of carbon doping on the mesoporous structure of nanocrystalline titanium dioxide and its solar-light-driven photocatalytic degradation of NO_x, Langmuir 24 (2008) 3510–3516.
[4] C.H. Ao, S.C. Lee, Indoor air purification by photocatalyst TiO_2 immobilized on an activated carbon filter installed in an air cleaner, Chem. Eng. Sci. 60 (2005) 103–109.
[5] C.H. Ao, S.C. Lee, S.C. Zou, Inhibition effect of SO_2 on NO_x and VOCs during the photodegradation of synchronous indoor air pollutants at parts per billion (ppb) level by TiO_2, Appl. Catal. B: Environ. 49 (2004) 187–193.
[6] C.H. Ao, S.C. Lee, Combination effect of activated carbon with TiO_2 for the photodegradation of binary pollutants at typical indoor air level, J. Photochem. Photobiol. A: Chem. 161 (2004) 2–3.
[7] J.G. Yu, X.X. Yu, Hydrothermal synthesis and photocatalytic activity of zinc oxide hollow spheres, Environ. Sci. Technol. 42 (2008) 4902–4907.
[8] M.A. Fox, M.T. Dulay, Heterogeneous photocatalysis, Chem. Rev. 93 (1993) 341–357.
[9] M.R. Hoffmann, S.T. Martin, W. Choi, D.W. Bahnemann, Environmental applications of semiconductor photocatalysis, Chem. Rev. 95 (1995) 69–96.
[10] F.B. Li, X.Z. Li, C.H. Ao, M.F. Hou, S.C. Lee, Photocatalytic conversion of NO using TiO_2–NH_3 catalysts in ambient air environment, Appl. Catal. B: Environ. 54 (2004) 275–283.
[11] W.K. Ho, J.C. Yu, S.C. Lee, Photocatalytic activity and photo-induced hydrophilicity of mesoporous TiO_2 thin films coated on aluminum substrate, Appl. Catal. B: Environ. 73 (2007) 135–143.
[12] Z.B. Wu, S. Guo, H.Q. Wang, Y. Liu, Synthesis of immobilized TiO_2 nanowires by anodic oxidation and their gas phase photocatalytic properties, Electrochem. Commun. 11 (2009) 1692–1695.
[13] R. Mendez-Roman, N. Cardona-Martinez, Relationship between the formation of surface species and catalyst deactivation during the gas-phase photocatalytic oxidation of toluene, Catal. Today 40 (1998) 353–365.
[14] G. Martra, S. Coluccia, L. Marchese, The role of H_2O in the photocatalytic oxidation of toluene in vapour phase on anatase TiO_2, Catal. Today 53 (1999) 695–702.
[15] X.T. Shen, L.H. Zhu, C.X. Huang, H.Q. Tang, Z.W. Yu, F. Deng, Inorganic molecular imprinted titanium dioxide photocatalyst: synthesis, characterization and its application for efficient and selective degradation of phthalate esters, J. Mater. Chem. 19 (2009) 4843–4851.
[16] S. Malato, J. Caceres, A.R. Fernandez-Alba, L. Piedra, M.D. Hernando, A. Aguera, J. Vial, Photocatalytic treatment of diuron by solar photocatalysis: evaluation of main intermediates and toxicity, Environ. Sci. Technol. 37 (2003) 2516–2524.
[17] E. Kowalska, H. Remita, C. Colbeau-Justin, J. Hupka, J. Belloni, Modification of titanium dioxide with platinum ions and clusters: application in photocatalysis, J. Phys. Chem. C 112 (2008) 1124–1131.
[18] A. Dawson, P.V. Kamat, Semiconductor-metal nanocomposites. Photoinduced fusion and photocatalysis of gold-capped TiO_2 (TiO_2/gold) nanoparticles, J. Phys. Chem. B 105 (2001) 960–966.
[19] P.D. Cozzoli, E. Fanizza, R. Comparelli, M.L. Curri, A. Agostiano, D. Laub, Role of metal nanoparticles in TiO_2/Ag nanocomposite-based microheterogeneous photocatalysis, J. Phys. Chem. B 108 (2004) 9623–9630.
[20] C.C. Chen, H.L. Bai, C.L. Chang, Effect of plasma processing gas composition on the nitrogen-doping status and visible light photocatalysis of TiO_2, J. Phys. Chem. C 111 (2007) 15228–15235.
[21] D. Mitoraj, H. Kisch, The nature of nitrogen-modified titanium dioxide photocatalysts active in visible light, Angew. Chem. Int. Ed. 47 (2008) 9975–9978.
[22] S. Sakthivel, H. Kisch, Daylight photocatalysis by carbon-modified titanium dioxide, Angew. Chem. Int. Ed. 42 (2003) 4908–4911.
[23] Y.Z. Li, X. Zhou, X.L. Hu, X.J. Zhao, P.F. Fang, Formation of surface complex leading to efficient visible photocatalytic activity and improvement of photostability of ZnO, J. Phys. Chem. C 113 (2009) 16188–16192.
[24] W.J. Ren, Z.H. Ai, F.L. Jia, L.Z. Zhang, X.X. Fan, Z.G. Zou, Low temperature preparation and visible light photocatalytic activity of mesoporous carbon-doped crystalline TiO_2, Appl. Catal. B: Environ. 69 (2007) 138–144.
[25] X. Zhao, Y.F. Zhu, Synergetic degradation of rhodamine B at a porous $ZnWO_4$ film electrode by combined electro-oxidation and photocatalysis, Environ. Sci. Technol. 40 (2006) 3367–3372.
[26] J.W. Tang, Z.G. Zou, J.H. Ye, Efficient photocatalysis on $BaBiO_3$ driven by visible light, J. Phys. Chem. C 111 (2007) 12779–12785.
[27] F. Gao, X.Y. Chen, K.B. Yin, S. Dong, Z.F. Ren, F. Yuan, T. Yu, Z.G. Zou, J.M. Liu, Visible-light photocatalytic properties of weak magnetic $BiFeO_3$ nanoparticles, Adv. Mater. 19 (2007) 2889–2892.
[28] B.B. Kale, J.O. Baeg, S.M. Lee, H. Chang, S.J. Moon, C.W. Lee, $CdIn_2S_4$ nanotubes and "Marigod" nanostructures: a visible-light photocatalyst, Adv. Funct. Mater. 16 (2006) 1349–1354.
[29] L.Z. Zhang, I. Djerdj, M.H. Cao, M. Antonietti, M. Niederberger, Nonaqueous sol–gel synthesis of nanocrystalline $InNbO_4$ visible light photocatalyst, Adv. Mater. 19 (2007) 2083–2086.
[30] Z.H. Ai, W.K. Ho, S.C. Lee, Efficient photocatalytic removal of NO in indoor air with hierarchical bismuth oxybromide nanoplate microspheres under visible light, Environ. Sci. Technol. 43 (2009) 4143–4150.

[31] H.F. Lin, S.C. Liao, S.W. Hung, C.T. Hu, Thermal plasma synthesis and optical properties of Zn_2SnO_4 nanopowders, Mater. Chem. Phys. 117 (2009) 9–13.
[32] J. Zeng, M.D. Xin, K.W. Li, H. Wang, H. Yan, W.J. Zhang, Transformation process and photocatalytic activities of hydrothermally synthesized Zn_2SnO_4 nanocrystals, J. Phys. Chem. C 112 (2008) 4159–4167.
[33] M.A. Alpuche-Aviles, Y.Y. Wu, Photoelectrochemical study of the band structure of Zn_2SnO_4 prepared by the hydrothermal method, J. Am. Chem. Soc. 131 (2009) 3216–3224.
[34] J.X. Wang, X.W. Sun, S.S. Xie, W.Y. Zhou, Y. Yang, Single-crystal and twinned Zn_2SnO_4 nanowires with axial periodical structures, Cryst. Growth Des. 8 (2008) 207–210.
[35] B. Tan, E. Toman, Y.G. Li, Y.Y. Wu, Zinc stannate (Zn_2SnO_4) dye-sensitized solar cells, J. Am. Chem. Soc. 129 (2007) 4162–4163.
[36] A. Rong, X.P. Gao, G.R. Li, T.Y. Yan, H.Y. Zhu, J.Q. Qu, D.Y. Song, Hydrothermal synthesis of Zn_2SnO_4 as anode materials for Li-ion battery, J. Phys. Chem. B 110 (2006) 14754–14760.
[37] Y. Ohko, Y. Nakamura, A. Fukuda, S. Matsuzawa, K. Takeuchi, Photocatalytic oxidation of nitrogen dioxide with TiO_2 thin films under continuous UV-light illumination, J. Phys. Chem. C 112 (2008) 10502–10508.
[38] J.L. Shie, C.H. Lee, C.S. Chiou, C.T. Chang, C.C. Chang, C.Y. Chang, Photodegradation kinetics of formaldehyde using light sources of UVA, UVC and UVLED in the presence of composed silver titanium oxide photocatalyst, J. Hazard. Mater. 155 (2008) 164–172.
[39] M. Sun, D.Z. Li, W.J. Zhang, Z.X. Chen, H.J. Huang, W.J. Li, Y.H. He, X.Z. Fu, Photocatalyst $Cd_2Sb_2O_{6.8}$ with high photocatalytic activity toward benzene and dyes, J. Phys. Chem. C 113 (2009) 14916–14921.
[40] S. Yin, B. Liu, P. Zhang, T. Morikawa, K.I. Yamanaka, T. Sato, Photocatalytic oxidation of NO_x under visible LED light irradiation over nitrogen-doped titania particles with iron or platinum loading, J. Phys. Chem. C 112 (2008) 12425–12431.